Palaeogeography, Palaeoclimatology, Palaeoecology 546 (2020) 109676

Contents lists available at ScienceDirect

Palaeogeography, Palaeoclimatology, Palaeoecology

journal homepage: www.elsevier.com/locate/palaeo

Spatiotemporal evolution and causes of marine euxinia in the early Cambrian Nanhua Basin (South China)

Chao Li[a,*], Zihu Zhang[a], Chengsheng Jin[b], Meng Cheng[a], Haiyang Wang[a], Junhua Huang[c], Thomas J. Algeo[a,c,d]

[a] State Key Laboratory of Biogeology and Environmental Geology, China University of Geosciences, Wuhan 430074, China
[b] Yunnan Key Laboratory for Palaeobiology, Yunnan University, Kunming 650091, China
[c] State Key Laboratory of Geological Processes and Mineral Resources, China University of Geosciences, Wuhan 430074, China
[d] Department of Geology, University of Cincinnati, Cincinnati 45221-0013, USA

ARTICLE INFO

Editor: Thomas Algeo

Keywords:
Redox
Sulfur cycling
Chemical weathering
CIA
Cathaysia Block
Yangtze Block

ABSTRACT

Marine redox conditions and their dynamic variations in the early Cambrian are thought to have strongly influenced the evolution of early animals. However, the patterns and mechanisms of contemporaneous marine redox variation remain poorly understood. The Nanhua Basin (South China) was a failed rift basin located between the Yangtze Block (NW margin) and Cathaysia Block (SE margin) in the early Cambrian. In this study, we conducted a comprehensive study of marine redox conditions, sulfur cycling, and chemical weathering intensity of source areas for the lower Cambrian shales of the Qingxi Formation in the basinal Shimensuidao section, which was geographically close to the Cathaysia Block. We integrated these results with previously published data from the nearby Silikou section as well as the coeval inner-shelf Xiaotan, upper-slope Daotuo, lower-slope Longbizui, and basinal Zhalagou sections, where were closer to the Yangtze Block. At Shimensuidao, iron species and redox-sensitive trace element data suggest dominantly euxinic conditions for the organic-rich black shale interval (lower member; LM) and variable redox conditions (oxic-ferruginous-euxinic) for the overlying organic-lean shales (upper member; UM) of the Qingxi Formation. Integrated redox results show a similar lessening of euxinic conditions from LM to UM across the entire basin and that euxinia developed along both the Yangtze and Cathaysia basin margins, but it was mainly in upper-slope areas (e.g., Daotuo) on the Yangtze margin and reached basinal areas (e.g., Silikou and Shimensuidao) on the Cathaysia margin. A decline of $\delta^{34}S_{py}$ from LM to UM was observed at Shimensuidao and other sections, which can be explained by decreasing microbial sulfate reduction rates due to decreasing organic availability and increasing riverine sulfate flux at study sections. Lower $\delta^{34}S_{py}$ values in shallow-marine relative to deep-marine areas suggest increased terrestrial sulfate availability to the shallower sites. Chemical index of alteration (CIA) values at Shimensuidao are uniformly high for both the LM (CIA_{corr1}: 82.5 ± 0.4, CIA_{corr2}: 88.6 ± 0.5) and UM (CIA_{corr1}: 80.2 ± 2.3, CIA_{corr2}: 86.2 ± 2.5) compared with the low-to moderate values at Daotuo (CIA_{corr2}: 61.9 ± 3.9 for LM, 71.3 ± 4.8 for UM). This pattern is consistent with intense chemical weathering of source areas on the Cathaysia Block and weaker chemical weathering of source areas on the Yangtze Block. Based on these observations, we propose that strong chemical weathering of the Cathaysia Block led to regionally high terrigenous sulfate fluxes, resulting in expansion of mid-depth euxinia into deep basinal areas on the Cathaysia margin of the Nanhua Basin. In contrast, weak chemical weathering of the Yangtze Block yielded lower terrigenous sulfate fluxes, limiting euxinia to upper slope areas on the Yangtze margin of the basin. Weaker euxinia during UM deposition may have been due to its decreasing organic availability and/or small seawater sulfate reservoir caused by persistent euxinic consumption during LM deposition. Our results highlight the complex controls and the key role of continental weathering and resulting terrigenous sulfate fluxes in marine euxinic variations in early Cambrian marginal seas, providing new insights into the co-evolution of continents, oceans, and early animals.

* Corresponding author.
E-mail address: chaoli@cug.edu.cn (C. Li).

https://doi.org/10.1016/j.palaeo.2020.109676
Received 7 October 2019; Received in revised form 20 January 2020; Accepted 22 February 2020
Available online 26 February 2020

1. Introduction

The "Cambrian Explosion," a rapid diversification of early animals during the early Cambrian (~541-509 Ma), coincided with a rise of oxygen in the oceanic system (e.g., Nursall, 1959; Knoll and Carroll, 1999; Li et al., 2017, 2018). However, the degree of oxygenation of early Cambrian oceans is uncertain. One hypothesis holds that early Cambrian oceans had oxygen levels close to those of the modern ocean, and that anoxia was primarily a local feature related to high primary productivity, comparable to modern oceanic oxygen minimum zones (X. Chen et al., 2015; Guilbaud et al., 2018; Wang et al., 2018). A second hypothesis argues that early Cambrian oceanic oxygen levels were far lower than in the modern ocean and closer to those of Precambrian oceans (e.g., Feng et al., 2014; Sperling et al., 2015; Jin et al., 2016; Li et al., 2017). Recently, a study of Fe^{3+} to total Fe ratios (Fe^{3+}/Fe_T) in hydrothermally altered basalts provided evidence that stepwise oceanic oxygenation commenced at the onset of the Cambrian (~541 Ma), but that deep-ocean oxygenation was delayed until the late Paleozoic (< 420 Ma; Stolper and Keller, 2018), supporting low oceanic oxygen levels in early Cambrian deep oceans. A number of studies have further inferred spatially heterogeneous redox conditions in early Cambrian oceans, which were characterized by a mid-depth euxinic watermass that dynamically coexisted with oxic surface waters and ferruginous deep waters (e.g., Feng et al., 2014; Wen et al., 2014; Sperling et al., 2015; Jin et al., 2014, 2016; Chang et al., 2018; Zhang et al., 2018). These studies have commonly linked metazoan diversification and ecological expansion during the early Cambrian to oceanic oxygenation via pulsed or stepwise oxic expansion from surface waters of continental shelves into the deeper water column, causing the toxic mid-depth "euxinic wedge" to shrink (Jin et al., 2014, 2016; Cheng et al., 2017; Dahl et al., 2017; Li et al., 2017; Xiang et al., 2017; Wei et al., 2018). Thus, marine shelf redox variations are likely to have been more important than those in the deep ocean for understanding the relationship between ocean-early animal co-evolution (Li et al., 2018).

The development of euxinia depends on the relative fluxes of hydrogen sulfide (H_2S) and reactive iron in the system, with H_2S production regulated by the availability of organic carbon and dissolved sulfate, which are linked via a microbially mediated redox couple (Raiswell and Canfield, 2012). Sulfate is supplied to the oceans mainly through weathering and oxidation of sulfides on land (Canfield and Raiswell, 1999; Fakhraee et al., 2019). Rising oxygen levels are thought to have led to pronounced increases in seawater sulfate concentrations during the Neoproterozoic and late Paleozoic (Algeo et al., 2015; He et al., 2019). However, owing to generally low concentrations (Loyd

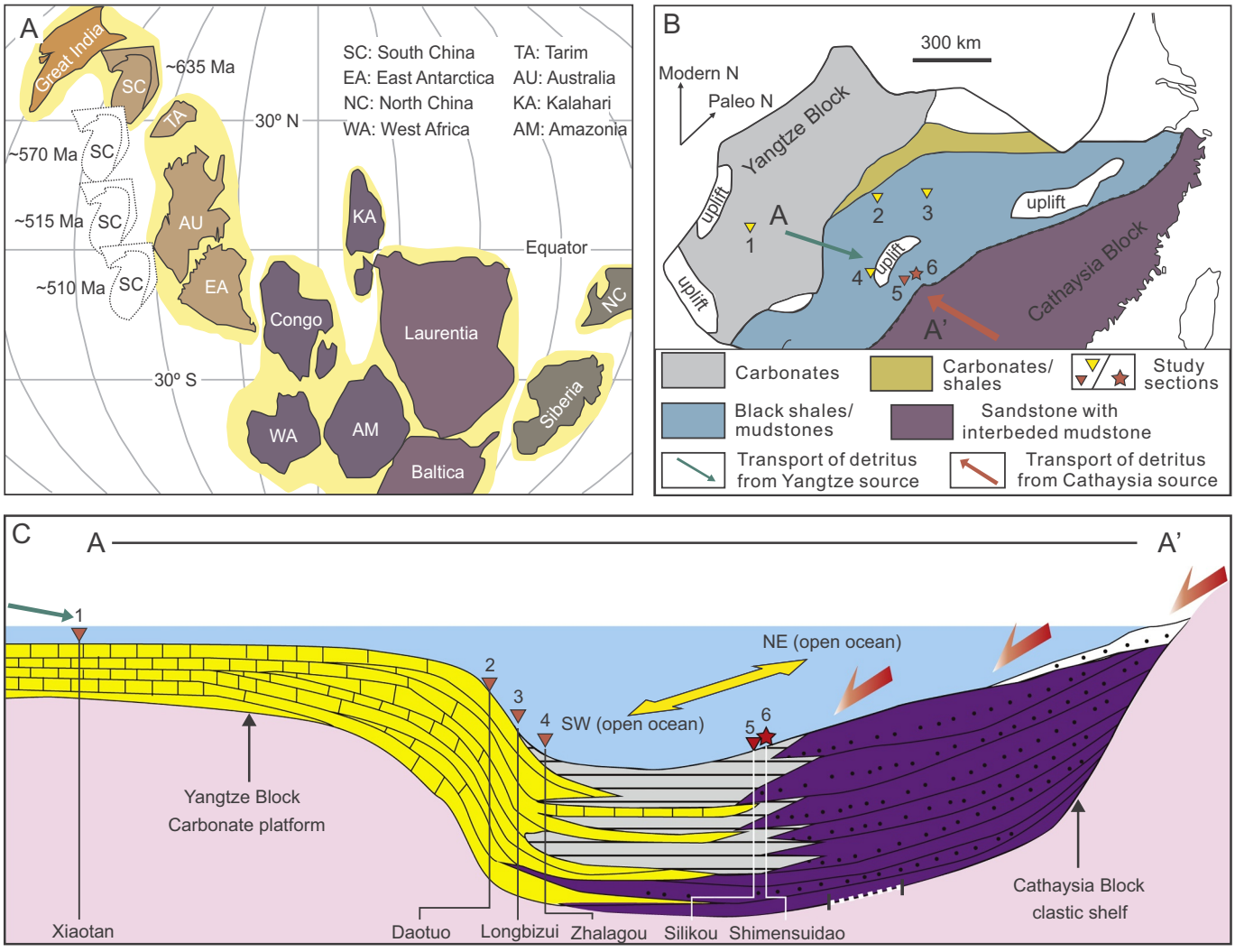

Fig. 1. Geological framework of lower Cambrian study sections. (A) Global paleogeographic reconstruction (modified from Zhang et al., 2015). (B) Paleogeographic map of the South China Block (modified from Goldberg et al., 2007). (C) Cross-section of South China Block (modified from Wang et al., 2010). The dashed line marked on the seafloor prior to deposition indicates the uncertainty of distance to land margin of the Cathaysia Block. Sections: 1-Xiaotan, 2-Daotuo, 3-Longbizui, 4-Zhalagou, 5-Silikou, 6-Shimensuidao.

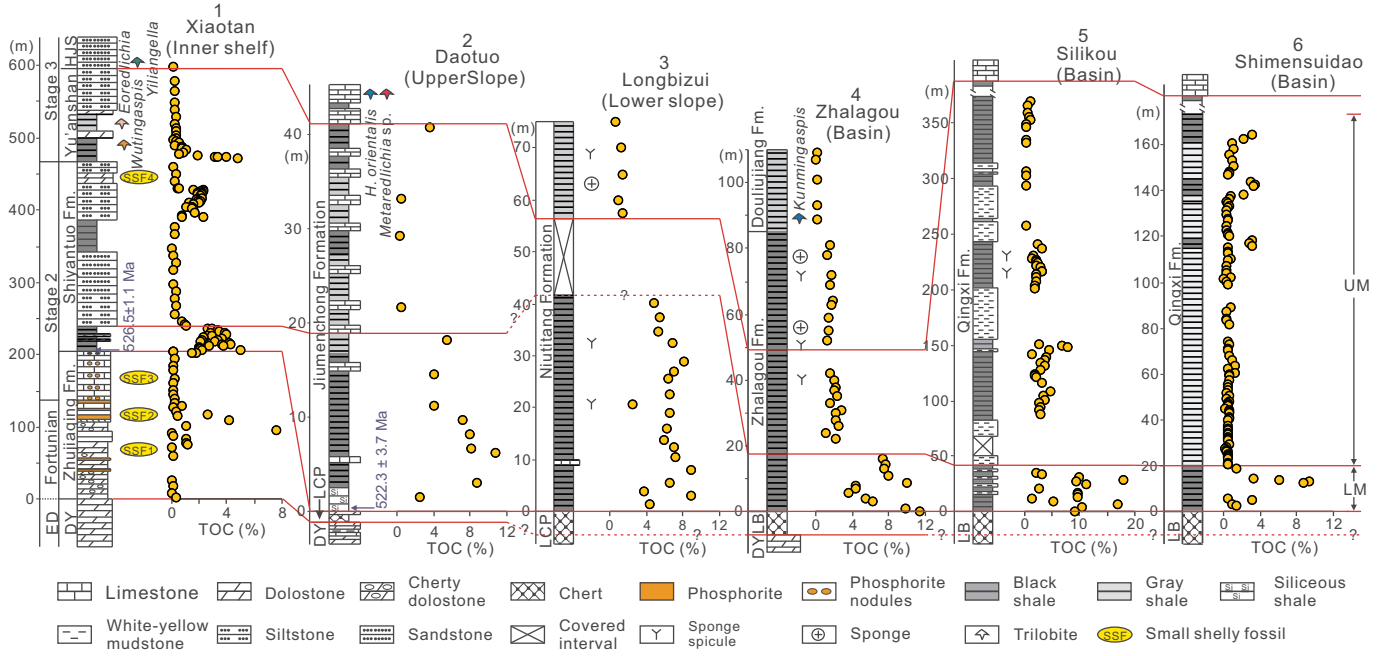

Fig. 2. Stratigraphic correlation of lower Cambrian strata in Nanhua Basin. Data sources: 1-Xiaotan (Zhu et al., 2001; Cremonese et al., 2013; Och et al., 2013); 2-Daotuo (Yang et al., 2003; Zhai et al., 2018); 3-Longbizui (J. Wang et al., 2012; Guo et al., 2013); 4-Zhalagou (Li et al., 2017); 5-Silikou (Zhang et al., 2018); 6-Shimensuidao (this study). U—Pb ages for the Xiaotan and Daotuo sections are from the adjacent Meishucun (Compston et al., 2008) and Bahuang sections (D. Chen et al., 2015), respectively. Abbreviations: ED = Ediacaran, DY = Dengying Formation, HJS = Hongjinshao Formation, LCP = Liuchapo Formation, LB = Laobao Formation, LM = Lower member, UM = Upper member.

et al., 2012), oceanic sulfate was likely inhomogenously distributed, leading to spatial variations in microbial sulfate reduction (MSR) and local development of watermass euxinia in early Cambrian oceans (Feng et al., 2014). Although previous studies suggested possible links between development of mid-depth euxinia and terrigenous sulfate fluxes (e.g., Feng et al., 2014; Jin et al., 2014, 2016; Li et al., 2010, 2015a), the details of this connection remain poorly documented.

Lower Cambrian strata in South China are relatively continuous, widely exposed, and well preserved and thus make excellent targets for analysis of early Cambrian redox changes and their underlying mechanisms (Zhu et al., 2003; Jin et al., 2016). These strata have been the subject of many recent investigations that provide a detailed geological framework for the present study (see review in Zhu, 2010, Zhu et al., 2016, and references therein). In this study, we conducted a comprehensive analysis of marine redox conditions, sulfur cycling, and chemical weathering of source areas for lower Cambrian shales of the Shimensuidao section in the Nanhua Basin (South China). In combination with previously published data for other sections representing a range of water depths and geographic locales within the Nanhua Basin, our results provide new insights into spatiotemporal patterns of marine euxinia in the early Cambrian Nanhua Basin and its causes, which are of significance for understanding co-evolutionary relationships among continental weathering, seawater chemistry, and early animal evolution.

2. Geological setting

2.1. Paleogeography and lithostratigraphy

The South China Craton as an isolated microcontinent (Yao et al., 2014) shifted gradually from a mid-latitude position during the Ediacaran (~635 Ma) to the paleoequator by the early Cambrian (~510 Ma; Fig. 1A; Zhang et al., 2015). It was composed of the Yangtze and Cathaysia blocks (Fig. 1B). The Nanhua Basin, located between these blocks, developed as a failed intracontinental rift basin at ~820 Ma (Fig. 1B; Wang and Li, 2003). It is thought to have been connected to the open ocean during the early Cambrian at its northeastern and southwestern ends (note: all cited orientations are for the modern; Fig. 1B–C; Wang and Li, 2003). Such an inference is supported by (1) near-simultaneous appearance of small shelly fossil assemblages and arthropods in South China and other cratons globally (Steiner et al., 2007; Vannier et al., 2014; Yang et al., 2016); (2) similar carbonate carbon isotopic ($\delta^{13}C_{carb}$) profiles for the Cambrian Fortunian and Stage 2 in South China and other cratons globally (Ishikawa et al., 2008; Fan et al., 2011).

On the Yangtze Block, a series of NE-SW-trending facies belts were present, from proximal (NW) to distal (SE): (1) carbonate inner-shelf deposits; (2) interbedded carbonate and shale deposits of outer-shelf facies; and (3) shale/mudstone deposits of slope-basinal facies (Fig. 1B; Steiner et al., 2007; Zhu et al., 2007; Jiang et al., 2012). On the SE margin of the Nanhua Basin, the Cathaysia Block shed voluminous siliciclastics, including shale, siltstone, arkosic sandstone, quartz sandstone, and gravelly sandstone into the basin with no clear development of sedimentary facies belts (Fig. 1B–C; Yao et al., 2014).

The study section at Shimensuidao (25°51′21″N, 109°43′49″E) is in northeastern Sanjiang Dong Autonomous County, northern Guangxi Zhuang Autonomous Province, South China. It was located in the basinal area of the Nanhua Basin but closer to the Cathaysia Block than to the Yangtze Block during the early Cambrian (Fig. 1B–C). However, the distance of the study section from the coastline of the Cathaysia Block is uncertain due to the absence of sedimentological evidence (Fig. 1C). The section contains the upper Ediacaran Laobao Formation, which is composed of chert and siliceous shale, conformably overlain by the lower Cambrian Qingxi Formation. The latter formation consists of organic-rich shales with total organic carbon (TOC) content up to 9.4% in its lower part, organic-poor shale (generally TOC content < 0.5%) interbedded with three black shale layers in its middle part, and carbonate deposits in its upper part (Fig. 2). We accordingly divide the study shale strata of the Qingxi Formation into two members based on lithology for convenience of discussion later: (1) a lower member (LM;

0–20 m) consisting of the organic-rich black shale, and (2) an upper member (UM, 20–175 m) consisting of the organic-poor shale with three black shale layers (Fig. 2).

2.2. Regional stratigraphic correlation

Regional correlation of deep-water strata in the early Cambrian Nanhua Basin is challenging due to the absence of high-resolution radiometric data and index fossils. However, a general regional correlation framework has been developed based on available lithostratigraphic, biostratigraphic, radiometric and TOC data (Fig. 2; Jin et al., 2016). Placement of the Ediacaran-Cambrian boundary at the basal Laobao Formation (or stratigraphically equivalent Liuchapo Formation) is based on (1) a lithologic shift from dolomite of the upper Ediacaran Dengying Formation to chert of the basal Liuchapo and Laobao formations in the Daotuo and Zhalagou sections (Fig. 2; Zhai et al., 2018; Li et al., 2017), (2) Zircon U—Pb ages of 542.1 ± 5.0 Ma at the base of the Liuchapo Formation in the Ganziping section (Hunan Province), and 542.6 ± 3.7 Ma in the upper Liuchapo Formation in the Bahuang section (Guizhou Province) (D. Chen et al., 2015).

A series of U—Pb ages from the base of the lower Cambrian black shale succession on the Yangtze Platform suggests that this lithologic horizon can be used as a correlation marker: 526.5 ± 1.1 Ma at Meishucun, Yunnan Province (Compston et al., 2008), 526.4 ± 5.4 Ma at Yangtze Gorges, Hubei Province (Okada et al., 2014), 524.2 ± 5.1 Ma at Panmen, Guizhou Province (D. Chen et al., 2015), 522.3 ± 3.7 Ma at Bahuang, Guizhou Province (D. Chen et al., 2015), and 522.7 ± 4.9 Ma at Taoying, Guizhou Province (X. Wang et al., 2012). These U—Pb ages suggest that deposition of the black shale succession on the Yangtze Platform commenced during Cambrian Age 2 (~529–521 Ma).

A significant decrease in TOC contents of the siliciclastic/shale succession is seen at the end of organic-rich black shales in all study sections including the fossiliferous Xiaotan section, which provides an age constrain of middle Age 2 of the early Cambrian (Fig. 2). This TOC decrease likely represents the start of a major marine regression in the Nanhua Basin (Jin et al., 2020), making the TOC decline of the siliciclastic/shale succession a possible correlation marker across the Nanhua Basin.

A major lithological shift from shale to coarse-grained siliciclastic or carbonate deposits is seen in Xiaotan, Daotuo, Silikou and Shimensuidao sections, which likely represents the peak of the major marine regression during early Age 3 of the early Cambrian (Jin et al., 2020), making the base of the carbonate/coarse-grained siliciclastic deposits a correlation marker (Jin et al., 2016). This lithological shift was accompanied by a biological shift from simple small shelly fauna to complex trilobites such as *Hupeidiscus orientalis* and *Metaredlichia* sp. in the upper Niutitang/Jiumenchong Formation of the Weng'an section (Jin et al., 2016) and Daotuo section (note: the fossil data shown are from the nearby Songtao section; Yang et al., 2003), and to the third trilobite zone (*Yunnanaspis-Yiliangella*) of early Age 3 of the early Cambrian (~521–514 Ma) in the Xiaotan section (Yuan and Zhao, 1999; Na and Kiessling, 2015). Although the lithological transition is not observed in the deep-water Longbizui and Zhalagou sections, a biological shift from small, simple sponge spicules to larger, more complex sponges was correlative with the faunal changes observed at Weng'an, Daotuo, and Xiaotan (Jin et al., 2016).

Based on these radiometric ages and stratigraphic correlations, the maximum depositional interval of the present study units in the Qingxi Formation at Shimensuidao is ~12.5 Myr (i.e., ~526.5–514 Ma), yielding a minimum average sedimentation rate of 14 m Myr^{-1} for the 175-m-thick shale succession (Fig. 2).

3. Background for proxies used in this study

Sedimentary Fe species have been widely used to reconstruct modern and ancient marine redox conditions (e.g., Canfield et al., 2008; Li et al., 2010; Poulton and Canfield, 2011; note that all redox conditions mentioned in this study denote those of marine bottom waters unless indicated otherwise). Highly reactive iron (Fe_{HR}) is made up of iron in carbonates (Fe_{carb}), oxides (Fe_{ox}), magnetite (Fe_{mag}), and pyrite (Fe_{py}). Marine sediments are generally characterized by $Fe_{HR}/Fe_T < 0.22$ and > 0.38 for oxic and anoxic conditions, respectively (Poulton and Canfield, 2011). If anoxic conditions are inferred, Fe_{Py}/Fe_{HR} ratios < 0.7–0.8 and > 0.7–0.8 are indicative of ferruginous and euxinic conditions, respectively (Poulton and Canfield, 2011). Because samples with $Fe_T < 0.5\%$ are unreliable for assessment of Fe speciation (e.g., Clarkson et al., 2014), we limited Fe speciation analysis to samples with $Fe_T > 0.5\%$ in this study.

Redox-sensitive trace elements (RSTEs) have also been frequently used for evaluating modern and ancient redox conditions. Under oxic conditions, Mo is present as molybdate (MoO_4^{2-}), which is converted to particle-reactive thiomolybdates ($MoS_{4-x}O_x^{2-}$, x = 0–3) in the presence of H_2S; U is present as U^{6+}, which is converted to U^{4+} around the Fe(II)-Fe(III) redox boundary; and V is present as V^{5+}, which is converted to V^{4+} and V^{3+} under suboxic and euxinic conditions, respectively (Algeo and Maynard, 2004; Tribovillard et al., 2006). The reduced species of these RSTEs are generally less soluble and readily scavenged by the sediment, resulting in enrichments relative to average upper continental crust (Tribovillard et al., 2006). In addition to local redox conditions, the RSTE content of global and/or local seawater also influences their degree of sedimentary authigenic enrichment (Algeo and Lyons, 2006).

Pyrite sulfur isotopic compositions ($\delta^{34}S_{py}$) can be used to infer ancient marine sulfur cycling (e.g., Sperling et al., 2013). Fluctuations in $\delta^{34}S_{py}$ are mainly related to the isotopic composition of parent sulfate ($\delta^{34}S_{sulf}$) and fractionation during microbial sulfate reduction (ε_{MSR}) (Feng et al., 2014). MSR yields sulfide (H_2S and resulting pyrite) that is depleted in ^{34}S relative to parent sulfate (Habicht et al., 2002). Although there are many factors controlling ε_{MSR} in natural systems (e.g., Canfield and Teske, 1996; Habicht et al., 2002; Leavitt et al., 2013; Algeo et al., 2015), organic carbon and sulfate availabilities may be first-order controls because organic carbon and sulfate are limited reactants during MSR (Habicht et al., 2002; Leavitt et al., 2013). Usually, increasing organic carbon and decreasing sulfate availability will cause smaller ε_{MSR} and, in turn, higher $\delta^{34}S_{py}$ values (Habicht et al., 2002; Leavitt et al., 2013).

The chemical index of alteration (CIA) has been widely used to quantitatively evaluate the intensity of source-area weathering of detrital siliciclastics (Yan et al., 2019; Zhai et al., 2018). Low CIA values (< 70) are generally indicative of a low degree of chemical alteration likely under cold and arid climate conditions, whereas high CIA values (> 70) are indicative of a moderate-high degree of chemical alteration likely under warm and wet climate conditions (Scheffler et al., 2006; Rieu et al., 2007; Schoenborn and Fedo, 2011; Yan et al., 2019).

4. Materials and methods

A total of 108 fresh shale samples were collected for geochemical analyses from the newly exposed Shimensuidao profile. All potential weathered surfaces, post-depositional veins, and visible pyrite grains were removed from each sample, which was then cut into small pieces. The freshest pieces of ~100 g were crushed to powders using a tungsten carbide crusher (Retsch RS 200). TOC, total inorganic carbon (TIC), iron species, major and trace elements, and $\delta^{34}S_{py}$ were measured in the State Key Laboratory of Biogeology and Environmental Geology, China University of Geosciences (Wuhan).

For TOC analysis, ~500 mg of sample powder were acidified with 4-N HCl to remove inorganic carbon, neutralized to a pH of 7.0 by addition of deionized water, then dried overnight at ~50–60 °C. About 100 mg of sample residue were analyzed using a Jena multi-EA 4000 C—S analyzer for TOC content. About 100 mg of sample powder were

analyzed using the same C–S analyzer for total carbon content, and TIC was calculated by difference between total carbona and TOC. Analytical precision was better than ± 0.1% based on replicate analyses of Alpha Resources standard AR-4007 (total carbon = 7.62%).

Only the freshest samples were used for iron species analysis. The first three iron species were quantified using a sequential extraction procedure (Poulton and Canfield, 2005). About 100 mg of sample powder were extracted at 50 °C for 48 h under agitation using 1 M sodium acetate solution adjusted to a pH of 4.5 by addition of analytical-grade acetic acid for Fe_{carb}. The residue from the first step was extracted at 25 °C for 2 h under agitation using a 50 g/L sodium dithionite solution buffered to a pH of 4.8 by addition of 0.2 M sodium citrate and analytical-grade acetic acid for Fe_{ox}. The residue from the second step was extracted at 25 °C for 6 h under agitation using a 0.2 M ammonium oxalate and 0.17 M oxalic acid solution adjusted to a pH of 3.2 by addition of analytical-grade ammonia water for Fe_{mag}. All extracts were diluted using 2% nitric acid and analyzed for their Fe contents using an atomic absorption spectroscope (AAS) with a RSD of < 5%. Analytical errors were better than ± 0.15% for sequential extraction based on replicate analyses of two laboratory shale standards (CUG-2 and CUG-3; Li et al., 2015b). Fe_{py} contents were quantified using the Cr-reduction method of Canfield et al. (1986). Sample powders were treated under N_2 by addition of 20 ml of 12 N HCl and 40 ml of 1 M chromous chloride solution, and the mixture was heated for 2 h. The liberated hydrogen sulfide was trapped by 30 ml of 3% silver nitrate and 10% ammonia water to form Ag_2S precipitate, which was filtered, rinsed, dried, and weighed.

For $\delta^{34}S_{py}$ analysis, the dried Ag_2S precipitate was mixed with excess V_2O_5, and then measured using a Thermo-Fisher Scientific Delta V Plus isotope-ratio mass spectrometer coupled with a Flash elemental analyzer. Three IAEA standards (S1: $\delta^{34}S = -0.3‰$; S2: $\delta^{34}S = +22.7‰$; S3: $\delta^{34}S = -32.3‰$) were used to calibrate $\delta^{34}S_{py}$ values to V-CDT international standard and monitor data quality, and analytical errors were better than ± 0.2‰.

For trace elements, ~300 mg of sample powder was ashed at 850 °C for 8 h to remove volatiles prior to analysis. About 50 mg of each ashed sample were dissolved using a standard multi-acid digestion (HF-HNO_3-HCl; Li et al., 2010). After complete digestion, the solution was diluted in 2% nitric acid and measured using a quadrupole inductively coupled plasma mass spectrometer. USGS (BCR-2) and Chinese national standards (GBW07103 and GBW07104) were used to monitor data quality, and analytical errors were better than ± 5%. Enrichment factors (EF) for trace elements were calculated as $X_{EF} = (X/Al)_{sample}/(X/Al)_{UCC}$, in which X represents the targeted trace element (e.g., Mo, U, and V), and UCC is the average composition of upper continental crust (McLennan, 2001).

For major elements, ~200 mg of sample powder was dried at 105 °C for 2 h to remove moisture prior to analysis. About 0.6 mg of sample powder, ~6 g of a $Li_2B_4O_7$-$LiBO_2$-LiF mixture, and 0.3–0.4 g of ammonium nitrate were accurately weighed into a porcelain crucible. These solid particles were then completely mixed using a spatula, and then transferred to a platinum crucible. About 5 drops of lithium bromide solution were added into the mixture, and the platinum crucible was subsequently fused at 1080 °C for 10 min to form a glass bead. The glass bead was measured using an X-ray fluorescence spectrometer. Two Chinese national standards (GBW07107, GBW07108) were used to monitor data quality, with analytical errors better than ± 5%.

CIA is calculated as $CIA = molar\ [Al_2O_3/(Al_2O_3 + CaO^* + Na_2O + K_2O)] \times 100$, where CaO^* represents the CaO in silicate fraction. Because the study samples are characterized by low carbonate content (TIC < 0.7%; See the Supplementary information), CaO was corrected only for phosphate content using P_2O_5 data ($CaO^* = molar\ CaO - 10/3 \times P_2O_5$). For $CaO^* < Na_2O$, CaO^* was used directly for calculation of CIA, but for $CaO^* > Na_2O$, CaO^* was set equal to Na_2O to eliminate carbonate CaO influence (McLennan, 1993). K_2O was further corrected for K-metasomatism of the source rocks: $K_2O_{corr} = molar\ [m \times Al_2O_3 + m \times (CaO^* + Na_2O)]/(1–m)$, where $m = K_2O/(Al_2O_3 + CaO^* + Na_2O + K_2O)$ (Panahi et al., 2000). Two different corrected values were calculated owing to the inference of two different types of source rocks for the study samples (see Section 6.4): CIA_{corr1} (based on granite) and CIA_{corr2} (based on granodiorite).

5. Results

All geochemical data of the Shimensuidao study section are given in the Supplementary information, and stratigraphic patterns of key results are shown in Figs. 3 and 4. TOC ranges from 0 to 9.4% (mean 1.0%) [note: all reported ranges are minimum to maximum values]; Fe_T ranges from 0.5 to 6.6% (mean 3.4%); Fe_{HR}/Fe_T ranges from 0.1 to 1.0 (mean 0.4); Fe_{py}/Fe_{HR} ranges from 0 to 0.9 (mean 0.5); Mo ranges from 1.4 to 82.3 ppm (mean 8.8 ppm); Mo_{EF} ranges from 0.5 to 55.5 (mean 5.2); U ranges from 2.9 to 20.8 ppm (mean 6.1 ppm); U_{EF} ranges from 1.1 to 6.6 (mean 1.9); V ranges from 141 to 919 ppm (259 ppm); V_{EF} ranges from 1.1 to 10.0 (mean 2.2); $\delta^{34}S_{py}$ ranges from −19.6 to +23.6‰ (mean −9.9‰); Al ranges from 3.3 to 11.4% (mean 9.3%). CIA_{corr1} ranges from 76.1 to 83.5 (mean 80.4), and CIA_{corr2} ranges from 81.8 to 89.8 (mean 86.4). Values for most proxies are higher and more variable in the LM, whereas the UM shows lower and nearly uniform values. The only proxies that deviate from this pattern are Fe_T and Al, for which the LM yields lower values than the UM, and Mo_{EF}, for which values are similar in the LM and UM.

6. Discussion

6.1. Redox reconstruction for the Shimensuidao section

In the LM, samples with $Fe_T > 0.5\%$ are characterized by high Fe_{HR}/Fe_T (0.75–1.00; mean = 0.88) and moderate to high Fe_{py}/Fe_{HR} (0.41–0.93; mean = 0.81) (Fig. 3), suggesting dominantly euxinic conditions punctuated by ferruginous episodes. However, these samples are characterized by low Mo concentrations (1.4–11.2 ppm; mean = 5.4 ppm), low Mo_{EF} (0.8–8.7; mean = 3.8), U_{EF} (1.7–6.1; mean = 3.7), and V_{EF} (3.2–10; mean = 5.2) (Fig. 3). Although these low values for RSTEs are suggestive of suboxic conditions, minimal RSTE enrichments were also observed for ferruginous to euxinic shales from the coeval lower-slope Wuhe section of Guizhou Province (Sahoo et al., 2016). Thus, it is possible that low seawater RSTEs availability was a dominant influence on their limited sedimentary enrichment (see Section 3; Algeo and Lyons, 2006). Given high TOC and Fe-speciation values (Fig. 3 and Supplementary information), we interpret these limited RSTE enrichments in deep-water sections to have been the product of low global or local seawater trace-metal concentrations, with the latter condition linked to restriction of the Nanhua Basin (Sahoo et al., 2016).

In the UM, all samples with $Fe_T > 0.5\%$ show variable Fe_{HR}/Fe_T (0.10–1.00; mean = 0.35) and Fe_{py}/Fe_{HR} (0–0.92; mean = 0.52), suggesting variable redox conditions (i.e., oxic-ferruginous-euxinic). Such an inference is consistent with variable Mo concentrations (2–82.3 ppm; mean = 9.2 ppm) and RSTE enrichments [Mo_{EF}: (0.5–55.5; mean = 5.4); U_{EF}: (1.1–4; mean = 1.7); V_{EF}: (1.1–7.6; mean = 1.9)] (Fig. 3). Overall, the Shimensuidao section exhibits a shift toward less reducing and less euxinic conditions from the LM to the UM (Fig. 3).

6.2. Integrated redox evaluation of the early Cambrian Nanhua Basin

Within the regional stratigraphic framework for the lower Cambrian of the Nanhua Basin outlined in Section 2.2, we integrate our redox results at Shimensuidao with previous redox reconstructions for the coeval Xiaotan (inner shelf; Och et al., 2013), Daotuo (upper slope; Zhai et al., 2018), Longbizui (lower slope; J. Wang et al., 2012), Zhalagou (basin; Li et al., 2017), and Silikou (basin; Zhang et al., 2018) sections.

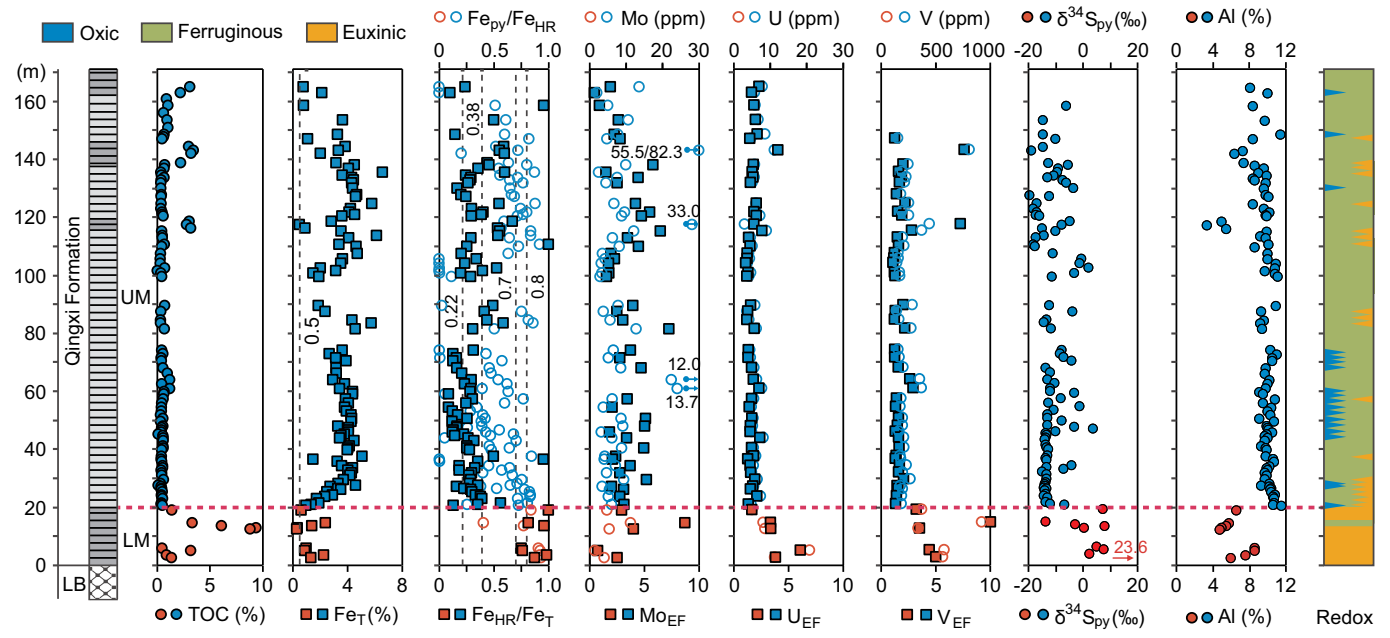

Fig. 3. Chemostratigraphic profiles of key geochemical proxies and redox summary for the Shimensuidao section. Dashed vertical lines represent key proxy threshold values (see text for discussion).

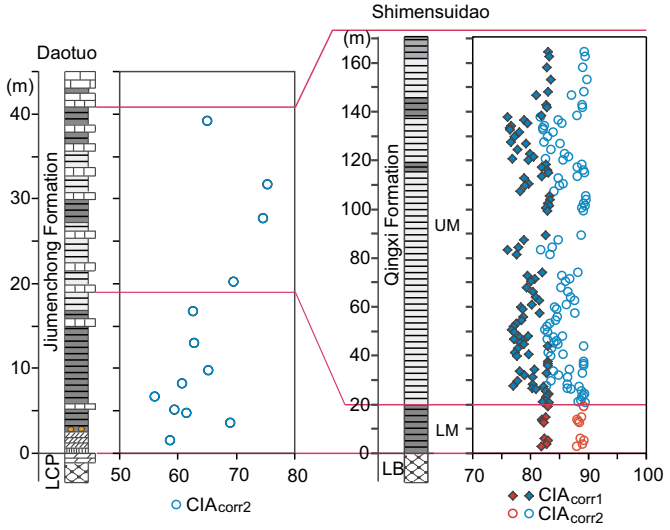

Fig. 4. Chemostratigraphic profiles of corrected CIA values for the Daotuo and Shimensuidao sections. CIA_{corr1} and CIA_{corr2} are values corrected for K-metasomatism based on granite and granodiorite, respectively. Data sources: Daotuo (Zhai et al., 2018) and Shimensuidao (this study). The stratigraphic correlation is taken from Fig. 2.

This integrated dataset allows assessment of spatiotemporal redox variation along a transect from the Yangtze Block to the Cathaysia Block, revealing two remarkable features (Fig. 5). First, mid-depth euxinic waters co-existed with oxic surface waters and ferruginous deep waters not only along the Yangtze margin, as suggested in previous studies (Feng et al., 2014; Jin et al., 2016), but also along the Cathaysia margin, particularly during deposition of the LM (i.e., the organic-rich black shale interval). However, the mid-depth euxinic watermass was more limited in extent on the Yangtze margin, being developed only on the upper slope (e.g., Daotuo), compared to the Cathaysia margin, where it extended into the basinal area (e.g., Silikou and Shimensuidao). Although redox data are lacking at present, the existence of a euxinic watermass between the observed euxinic basinal sites and oxic shallow sites can be inferred on the Cathaysia margin based on the euxinic wedge redox model of Li et al. (2010), which is regarded as generally applicable to the early Cambrian Nanhua Basin (Feng et al., 2014; Jin et al., 2016). Furthermore, euxinia may have extended into shallower areas on the Cathaysia margin due to ample sulfate and organic carbon availability (see Section 6.5). Therefore, we conclude that the first feature described here suggests a larger mid-depth euxinic watermass on the Cathaysia margin than the Yangtze margin of the early-Cambrian Nanhua Basin.

Second, a gradual weakening of euxinic conditions is observed upsection (i.e., from the LM to the UM) not only in the Shimensuidao section (Section 6.1) but across the entire Nanhua Basin (cf. Jin et al., 2016; Zhang et al., 2018; Zhai et al., 2018). Two mechanisms have been proposed for a long-term increase in oxygenation of the early Cambrian Nanhua Basin: (1) improving oceanic ventilation due to greater O_2 production in the early Cambrian (e.g., D. Chen et al., 2015; Jin et al., 2016; Dahl et al., 2017; Li et al., 2017, 2018); and (2) a sea-level fall within the Nanhua Basin (Peng et al., 2012), moving all sections into shallower, better-oxygenated surface waters (e.g., Zhang et al., 2018). However, neither mechanism readily explains the complex spatiotemporal pattern of euxinic variation observed across the early Cambrian Nanhua Basin, for which we explore possible additional mechanisms below.

6.3. Sulfur cycling in early Cambrian Nanhua Basin

$\delta^{34}S_{py}$ records can provide insights into sulfur cycling in the early Cambrian Nanhua Basin. Our results for the Shimensuidao section show a negative shift in $\delta^{34}S_{py}$ from the LM (−13.7‰ to +23.6‰; mean = +4.1‰) to the UM (−19.6‰ to +3.7‰; mean = −11.2‰) (Fig. 3). Shifts toward lower $\delta^{34}S_{py}$ values in the coeval inner-shelf Shatan, outer-shelf Jinsha and shelf-margin Yangjiaping sections have been linked to an enhanced flux of ^{34}S-depleted riverine sulfate (Feng et al., 2014; Jin et al., 2016). In addition, lower MSR rates owing to decreased organic carbon availability were inferred for the coeval outer-shelf Wangjiaping section (Jin et al., 2017). The MSR rate/organic carbon availability mechanism has some support at Shimensuidao based on a moderate positive correlation between $\delta^{34}S_{py}$ and TOC (r = +0.32, $p(\alpha)$ < 0.01; Fig. 6A). The ^{34}S-depleted riverine sulfate mechanism has an equal measure of support based on a moderate

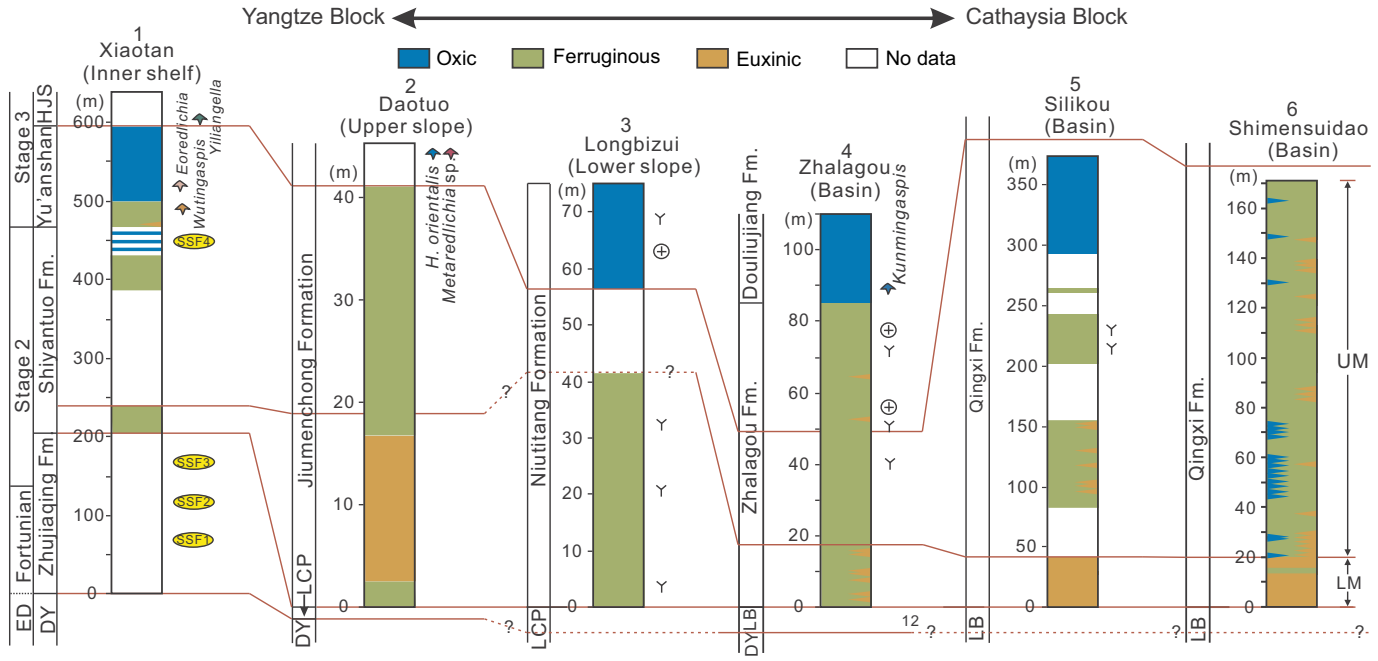

Fig. 5. Transect across the early Cambrian Nanhua Basin showing spatiotemporal redox variation along both the NW Yangtze margin and SE Cathaysia margin. Data sources: 1-Xiaotan (Och et al., 2013), 2-Daotuo (Zhai et al., 2018), 3-Longbizui (J. Wang et al., 2012), 4-Zhalagou (Li et al., 2017), 5-Silikou (Zhang et al., 2018), 6-Shimensuidao (this study). The stratigraphic correlation is taken from Fig. 2.

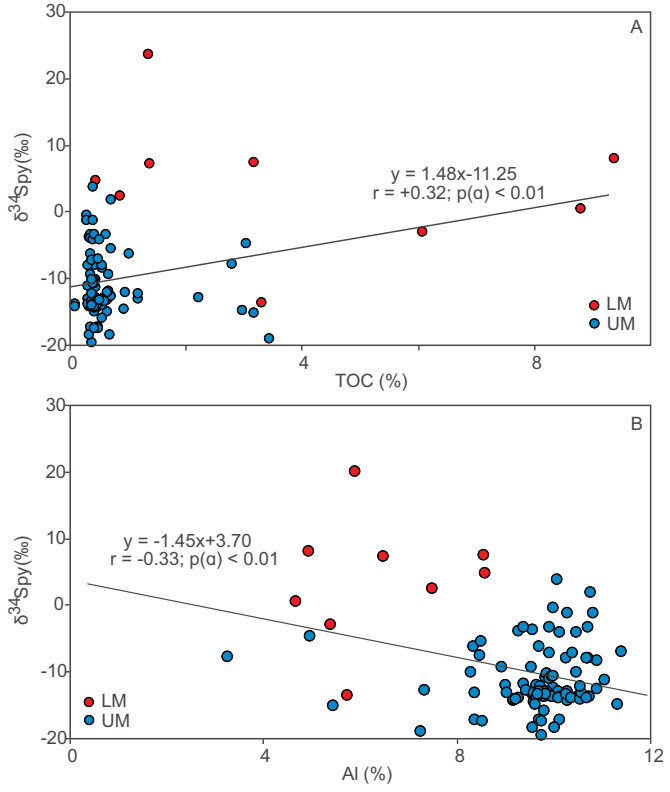

Fig. 6. Crossplots of $\delta^{34}S_{py}$ versus TOC (A) and Al concentrations (B) for the Shimensuidao section.

negative correlation between $\delta^{34}S_{py}$ and riverine fluxes, as proxied by Al ($r = -0.33, p(\alpha) < 0.01$; Fig. 6B). Therefore, changes in both MSR rates and riverine sulfate fluxes likely contributed to the decline of $\delta^{34}S_{py}$ from the LM to the UM at Shimensuidao and other sections in the Nanhua Basin.

In order to explore spatial patterns of sulfur cycling in the early Cambrian Nanhua Basin, we integrated $\delta^{34}S_{py}$ data from the organic-rich LM of Shimensuidao with published $\delta^{34}S_{py}$ data from correlative organic-rich black shales in other sections (Table 1 and Fig. 7). The integrated $\delta^{34}S_{py}$ dataset shows that deep-water/distal sections (e.g., Longbizui, Jinsha, and Wen'an) generally have heavier $\delta^{34}S_{py}$ values than shallow-water sections (e.g., Xiaotan and Shatan) on the Yangtze margin, even though all sections have high TOC values (Table 1). This pattern is consistent with the hypothesis that pyrite formation at shallower anoxic sites involved a greater proportion of ^{34}S-depleted riverine sulfate, as suggested in previous studies (Feng et al., 2014; Jin et al., 2016; Wang et al., 2020). In addition, despite similarly high TOC values (Table 1), the $\delta^{34}S_{py}$ of the LM from deep-water sections on the Cathaysia margin (e.g., Silikou and Shimensuidao) is much lower than that from deep-water sections on the Yangtze margin (e.g., Longbizui, Songtao and Wen'an; Table 1 and Fig. 7). This pattern implies that deep watermass on the Cathaysia margin was influenced by larger amounts of ^{34}S-depleted riverine sulfate than the deep watermass on the Yangtze margin.

6.4. Chemical weathering of source area and terrigenous fluxes to early Cambrian Nanhua Basin

In order to explore the degree of chemical weathering of source areas to the Yangtze and Cathaysia margins of the Nanhua Basin, we analyzed the CIA data of representative sections: Daotuo for the former (Zhai et al., 2018) and Shimensuidao for the latter (this study). Because K-metasomatism of shales can have a large effect on CIA values, we evaluated this effect using an Al_2O_3-(CaO^* + Na_2O)-K_2O (i.e., A-CN-K) ternary diagram (Fig. 8; Fedo et al., 1995). Theoretically, a series of CIA values are distributed along an ideal straight line parallel to the A-CN sideline in response to variable weathering intensity (McLennan, 1993). In contrast, CIA values deviated from the ideal weathering trend such as our study samples (Fig. 8), which is indicative of diagenetic K-metasomatism (Fedo et al., 1995; Rieu et al., 2007). The effects of diagenetic K-metasomatism can be corrected as shown in Section 4 based on the composition of the source rock of the study samples (Panahi et al.,

Table 1
Compilation of TOC and $\delta^{34}S_{py}$ data published for the lower Cambrian organic-rich black shales of the Nanhua Basin.

Section	Facies	Number	TOC (mean, %)	$\delta^{34}S_{py}$ (range, ‰)	$\delta^{34}S_{py}$ (mean, ‰)	Reference
Yangtze margin sections						
Xiaotan	Inner shelf	6	1.9	−17.5 to −3.7	−12.0	Och et al. (2013)
Shatan	Inner shelf	13	3.2	−6.8 to +23.0	+4.0	Goldberg et al. (2007)
Jinsha	Outer shelf	14	4.9	+12.0 to +39.4	+13.6	Jin et al. (2016)
Wangjiaping	Outer shelf	12	3.3	−10.7 to +3.9	−0.8	Jin et al. (2017)
Yangjiaping	Shelf margin	14	10.7	+1.7 to +17.5	+8.3	Feng et al. (2014)
Weng'an	Shelf margin	15	6.1	−5.8 to +23.8	+12.2	Jin et al. (2016)
Songtao	Upper slope	22	8.6	−5.0 to +27.0	+8.6	Goldberg et al. (2007)
Longbizui	Lower slope	19	6.2	+10.7 to +33.0	+21.0	J. Wang et al. (2012)
Cathaysia margin sections						
Silikou	Basin	7	8.5	−2.6 to +2.5	−1.7	Zhang et al. (2018)
Shimensuidao	Basin	9	3.9	−13.7 to +23.6	+4.1	This study

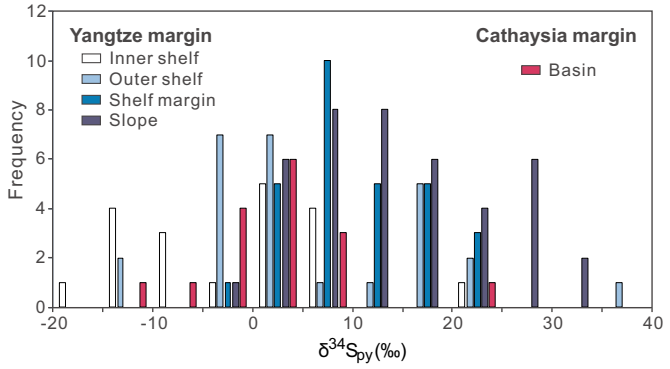

Fig. 7. Frequency distribution of $\delta^{34}S_{py}$ data from lower Cambrian organic-rich black shales in the Nanhua Basin. Data sources for Yangtze margin: inner shelf: Xiaotan (Och et al., 2013) and Shatan (Goldberg et al., 2007), outer shelf: Jinsha (Jin et al., 2016) and Wangjiaping (Jin et al., 2017), shelf margin: Yangjiaping (Feng et al., 2014) and Wen'an (Jin et al., 2016), slope: Songtao (Goldberg et al., 2007) and Longbizui (J. Wang et al., 2012). Data sources for Cathaysia margin: basin: Silikou (Zhang et al., 2018) and Shimensuidao (this study).

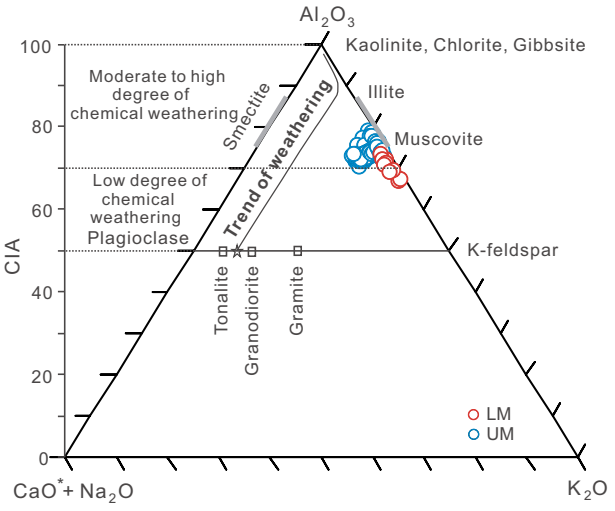

Fig. 8. Al_2O_3-(CaO^* + Na_2O)-K_2O ternary diagram showing diagenetic K-metasomatism of shales in the Shimensuidao section. Chemical index of alteration (CIA) ranges for different chemical weathering degrees are also indicated. LM = lower member, UM = upper member.

2000).

In order to correct for diagenetic K_2O, we conducted a source-rock-type analysis of the study sections. TiO_2 vs. Zr crossplots are useful for distinguishing igneous rock types (e.g., Hayashi et al., 1997; Zhai et al., 2018; Yan et al., 2019), with TiO_2/Zr ratios of < 55, 55–195, and > 195 indicative of felsic, intermediate, and mafic rocks, respectively (Hayashi et al., 1997). Our Daotuo and Shimensuidao samples are characterized by low TiO_2/Zr ratios (45.8 ± 6.9), suggesting that their source rocks are dominantly felsic in composition (Fig. 9A). La-Th-Sc diagram is also useful for discrimination of source rock types (Cullers and Podkovyrov, 2000). The study samples exhibit La-Th-Sc compositions consistent with both granite and granodiorite source rocks for Shimensuidao and mainly granodiorite source rocks for Daotuo (Fig. 9B). Therefore, corrections to CIA values for diagenetic K were based on typical Al_2O_3, CaO, Na_2O, K_2O, and P_2O_5 concentrations in granite (CIA_{corr1}) and granodiorite (CIA_{corr2}) source rocks for the Shimensuidao section, and granodiorite source rocks (CIA_{corr2}) for the

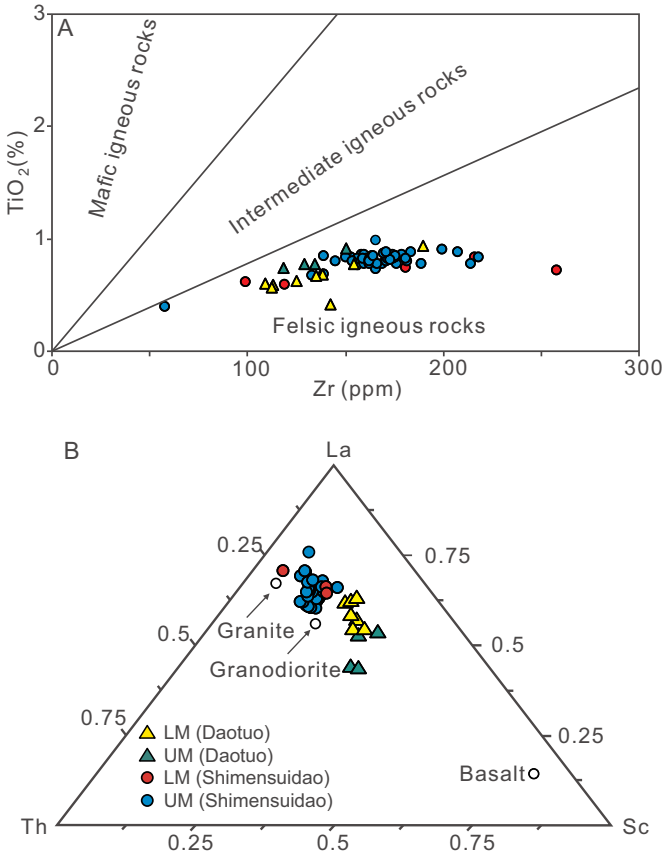

Fig. 9. Crossplot of TiO_2 versus Zr (A), and La-Sc-Th ternary diagram (B) showing source rock types for the Daotuo and Shimensuidao sections. LM = lower member, UM = upper member.

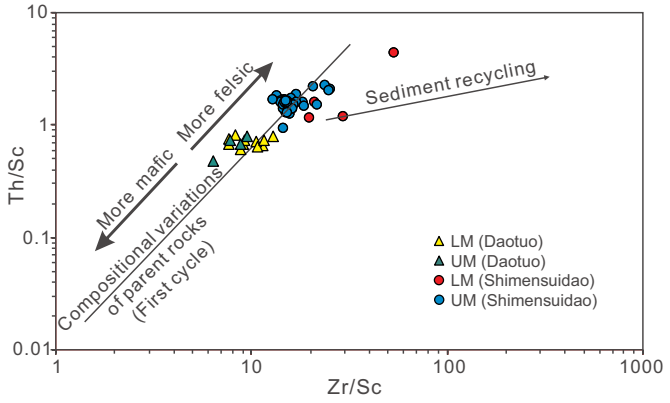

Fig. 10. Crossplot of Th/Sc versus Zr/Sc showing first-cycle condition of Shimensuidao and Daotuo sediments.

Daotuo section (Zhai et al., 2018).

Before applying CIA as a proxy for degree of chemical weathering in source areas, the possibility of sediment recycling must also be considered. Th/Sc vs. Zr/Sc crossplot is useful to evaluate this effect, with first-cycle sediments following the compositional variation trend of parent rocks and recycled sediments following a trend of zircon enrichments (Fig. 10; McLennan et al., 1993). The present study samples fall well in the compositional trend of parent rocks (except two outlier samples, Fig. 10), consistent with first-cycle sediments, thus allowing CIA values to be used as a proxy for degree of chemical weathering of the source areas.

The Shimensuidao section exhibits generally high CIA values (CIA_{corr1}: 82.5 ± 0.4, CIA_{corr2}: 88.6 ± 0.5; mean ± SD) for the LM and high but variable values for the UM (CIA_{corr1}: 80.2 ± 2.3, CIA_{corr2}: 86.2 ± 2.5) (Fig. 4). High CIA values suggest that its source rocks underwent intensive weathering likely under a warm and humid climate during accumulation of both the LM and UM. In contrast, the Daotuo section shows substantially low CIA_{corr2} values for the LM (61.9 ± 3.9) and low-moderate values for the UM (71.3 ± 4.8) (Fig. 4). These values indicate weak chemical weathering of the source area likely under relatively cooler and more arid conditions (Zhai et al., 2018), although chemical weathering intensity increased somewhat from the LM to the UM. The reasons for such a spatiotemporal pattern of chemical weathering intensity remain uncertain and need further investigation which is beyond of the scope of this study. Considering the similar but different source-rock types of the two representative sections (see above) and their locations relative to the Yangtze and Cathaysia margins (Fig. 1C), the spatiotemporal patterns of weathering intensity support that influx of terrigenous sediments to the Shimensuidao and Silikou sections was dominantly from the more-weathered Cathaysia Block, and fluxes to the Xiaotan, Daotuo, Longbizui, and Zhalagou sections were dominantly from the less-weathered Yangtze Block (Fig. 11; Wang et al., 2010; Yao et al., 2014, 2015; Zhai et al., 2018).

Physical erosion can facilitate the subaerial oxidation of sulfides and increase riverine sulfate fluxes through exposure of fresh rocks during glacial periods (Torres et al., 2017). Because there is no evidence for glacial conditions on the Yangtze and Cathaysia blocks during the early Cambrian, glacially enhanced physical erosion was probably not a significant influence on sulfate fluxes to the Nanhua Basin. Weathering of the source rocks of the Yangtze and Cathaysia blocks, which were granodiorite and/or granite (see above), would have required chemical decomposition of the silicate mineral matrix in order to expose the contained sulfides to air. Thus, we infer that chemical weathering was the dominant control on sulfate weathering fluxes to the early Cambrian Nanhua Basin. Accordingly, the varying chemical weathering intensities inferred for the Yangtze Block and Cathaysia Block sources areas of the study sections (see above) and the deep-water $\delta^{34}S_{py}$ pattern (see Section 6.3) both support larger amounts of ^{34}S-depleted riverine sulfate being delivered to the deep watermass from the Cathaysia margin than from the Yangtze margin.

6.5. Synthesis: a model for spatiotemporal evolution of marine euxinia in the early Cambrian Nanhua Basin

Based on the observations in Sections 6.3–6.4, we developed an integrated model to account for the spatiotemporal evolution of mid-depth euxinic watermass across the entire early Cambrian Nanhua Basin (see Section 6.2). As discussed in Section 1, development of euxinic conditions depends on the relative fluxes of H_2S (from MSR) and Fe_{HR} in the water column (Raiswell and Canfield, 2012). Fe_{HR} fluxes were likely high in the early Cambrian Nanhua Basin owing to abundant hydrothermal activities (cf. Jiang et al., 2007; Chen et al., 2009; Liu et al., 2015). Given a certain high Fe_{HR} flux, development of marine euxinia would have depended on generation of H_2S, which depends on both sulfate and organic matter availability (Feng et al., 2014). During deposition of the LM, organic matter was generally in ample supply as indicated by the high TOC values of these black shales, although organic matter availability may have been limited in areas such as the outer-shelf Wangjiaping section where TOC values are relatively low (Fig. 11A, Table 1, Jin et al., 2017). High TOC values indicate strong primary productivity, which was likely boosted by upwelling of nutrient-rich deep waters of the open ocean into the Nanhua Basin during an early Cambrian marine transgression (Jin et al., 2020). Under such conditions, euxinic waters were able to develop in areas with sufficient sulfate availability.

Previous study suggested two main sulfate sources for local sulfate supplies based on spatial heterogeneity of redox conditions and $\delta^{34}S_{py}$: the ^{34}S-rich ocean/basin sulfate reservoir, which was locally mixed with ^{32}S-rich riverine fluxes in shelf areas of the early Cambrian Nanhua Basin (Feng et al., 2014). The present compilation of $\delta^{34}S_{py}$ data for organic-rich black shales (i.e., the LM) in the Nanhua Basin supports this scenario (see Section 6.3). In combination with high organic availability in the Nanhua Basin, high sulfate fluxes due to intense chemical weathering of source areas on the Cathaysia Block (see Section 6.4) may have caused expansion of mid-depth euxinia toward basinal areas on the Cathaysia margin, as observed in the Shimenshuidao and Silikou sections (Fig. 11A). In contrast, low sulfate fluxes due to weak chemical weathering of source areas on the Yangtze Block resulted in more limited mid-depth euxinia on the Yangtze margin, which was mainly confined to upper-slope areas such as the Daotuo section (Fig. 11A).

During deposition of the UM, organic carbon availability was generally low as indicated by the low TOC content of these gray shales/siltstones/sandstones across the entire Nanhua Basin (Fig. 2). Reduced organic productivity was likely due to a decrease in nutrient fluxes from the open ocean as the Nanhua Basin became more isolated during a marine regression (Fig. 11B; Jin et al., 2020). In combination with strong MSR consumption of sulfate during earlier deposition of the LM (Feng et al., 2014), this regression limited the influx of open-ocean sulfate into the Nanhua Basin, which in turn limited overall sulfate availability in the basin. However, the sea-level fall may also have increased local riverine sulfate fluxes somewhat owing to enhanced weathering and terrigenous fluxes, as suggested by a large shift toward lower $\delta^{34}S_{py}$ values in the UM relative to the LM (see Section 6.3). The limited availability of organic matter and/or sulfate led to a strong reduction of mid-depth euxinia in the Nanhua Basin along with expansion of the oxic surface layer (Fig. 11B; also see Sections 6.2).

7. Conclusions

High-resolution profiles of Fe species, major and trace elements, C and S isotopes, and CIA data were generated for both organic-rich black

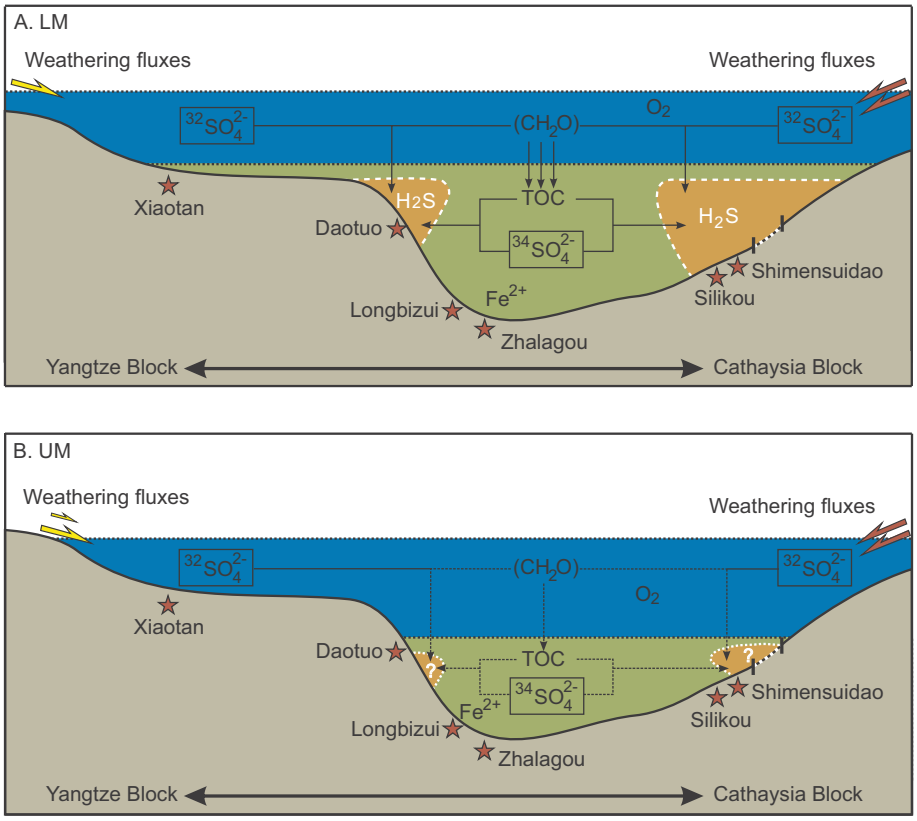

Fig. 11. Schematic model for spatiotemporal euxinic variation in the early Cambrian Nanhua Basin. (A) Terrestrial sulfate fluxes were a key control on the distribution of mid-depth euxinic waters on both basin margins during deposition of the lower member (LM). (B) Decreases in organic matter and/or sulfate availability resulted in weakening of marine euxinia in the basin during deposition of the UM. The dashed line marked on the seafloor indicates the uncertainty of distance to land margin of the Cathaysia Block. See text for details.

shales of the lower member (LM) and overlying organic-lean gray shales of the upper member (UM) of the lower Cambrian Shimensuidao section (South China), which was located in the basinal facies of the Nanhua Basin close to the Cathaysia Block. These new data were integrated with published results from the nearby Silikou section (basin) as well as from the coeval Xiaotan (inner shelf), Daotuo (upper slope), Longbizui (lower slope), Zhalagou (basin) sections, which were geographically closer to the Yangtze Block, in order to reconstruct the marine redox pattern, sulfur cycling, and chemical weathering intensities of source areas for the entire Nanhua Basin.

Our redox data provide the reconstruction of spatiotemporal redox variation across the entire early Cambrian Nanhua Basin from the northwest (Yangtze margin) to the southeast (Cathaysia margin). This reconstruction reveals (1) stronger development of mid-depth euxinia along the Cathaysia margin relative to the Yangtze margin during deposition of the LM, and (2) a weakening of mid-depth euxinia from the LM to the UM across the entire Nanhua Basin. The integrated $\delta^{34}S_{py}$ dataset demonstrates a strong spatial gradient in sulfate sources, with higher terrestrial sulfate fluxes in more proximal areas. CIA values are higher at Shimensuidao relative to Daotuo, consistent with more intense chemical weathering of source areas on the Cathaysia Block relative to the Yangtze Block. In light of these key observations and the results of Feng et al. (2014) and Jin et al. (2020), we propose that stronger chemical weathering of the Cathaysia Block resulted in higher terrigenous sulfate fluxes, providing ample sulfate that led to stronger mid-depth euxinia on the Cathaysia margin than the Yangtze margin during LM deposition. Reductions in organic matter and/or sulfate availability associated with a major marine regression were likely causes for contraction of mid-depth euxinia in the Nanhua Basin during UM deposition. Our study highlights the mechanistic complexity related to paleoceanographic, paleoclimatic and probably other factors, as well as the key roles of continental weathering and corresponding terrigenous sulfate fluxes on the spatiotemporal evolution of marine euxinia in the early Cambrian Nanhua Basin, providing new insights into the coevolution of continents, oceans, and early animals.

Supplementary data to this article can be found online at https://doi.org/10.1016/j.palaeo.2020.109676.

Declaration of competing interest

The authors declare no conflict of interest for the article of "Spatiotemporal evolution and causes of marine euxinia in the early Cambrian Nanhua Basin (South China)" by Chao Li et al.

Acknowledgments

We thank Hao Cui, Genming Luo, and Junhua Huang's group for field work and Biao Chang for laboratory assistance. We also thank Dr. Huan Cui and an anonymous reviewer for their constructive comments, which improved the manuscript. This study is supported by the National Natural Science Foundation of China-Research Councils UK-Natural Environment Research Council Program (grant 41661134048), National Natural Science Foundation of China (grants # 41825019, 41821001, 41902027), and the National Key Research and Development Program of China (grant 2016YFA0601100). Meng Cheng acknowledges support from the National Natural Science Foundation of China program (grant 41703008).

Data availability

Datasets related to this article can be found in the supplementary online material.

References

Algeo, T.J., Lyons, T.W., 2006. Mo-total organic carbon covariation in modern anoxic marine environments: Implications for analysis of paleoredox and paleohydrographic conditions. Paleoceanography 21, PA2016. https://doi.org/10.1029/2004pa001112.

Algeo, T.J., Maynard, J.B., 2004. Trace-element behavior and redox facies in core shales of Upper Pennsylvanian Kansas-type cyclothems. Chem. Geol. 206, 289–318.
Algeo, T.J., Luo, G.M., Song, H.Y., Lyons, T.W., Canfield, D.E., 2015. Reconstruction of secular variation in seawater sulfate concentrations. Biogeosciences 12, 2131–2151.
Canfield, D.E., Raiswell, R., 1999. The evolution of the sulfur cycle. Am. J. Sci. 299, 697–723.
Canfield, D.E., Teske, A., 1996. Late Proterozoic rise in atmospheric oxygen concentration inferred from phylogenetic and sulphur-isotope studies. Nature 382, 127–132.
Canfield, D.E., Raiswell, R., Westrich, J.T., Reaves, C.M., Berner, R.A., 1986. The use of chromium reduction in the analysis of reduced inorganic sulfur in sediments and shales. Chem. Geol. 54, 149–155.
Canfield, D.E., Poulton, S.W., Knoll, A.H., Narbonne, G.M., Ross, G., Goldberg, T., Strauss, H., 2008. Ferruginous conditions dominated later Neoproterozoic deep-water chemistry. Science 321, 949–952.
Chang, H., Chu, X., Feng, L., Huang, J., Chen, Y., 2018. Marine redox stratification on the earliest Cambrian (ca. 542–529 Ma) Yangtze Platform. Palaeogeogr. Palaeoclimatol. Palaeoecol. 504, 75–85.
Chen, D., Wang, J., Qing, H., Yan, D., Li, R., 2009. Hydrothermal venting activities in the Early Cambrian, South China: Petrological, geochronological and stable isotopic constraints. Chem. Geol. 258, 168–181.
Chen, D., Zhou, X., Fu, Y., Wang, J., Yan, D., 2015. New U–Pb zircon ages of the Ediacaran–Cambrian boundary strata in South China. Terra Nova 27, 62–68.
Chen, X., Ling, H.F., Vance, D., Shieldszhou, G.A., Zhu, M., Poulton, S.W., Och, L.M., Jiang, S.Y., Li, D., Cremonese, L., 2015. Rise to modern levels of ocean oxygenation coincided with the Cambrian radiation of animals. Nat. Commun. 6 art. 7142.
Cheng, M., Li, C., Zhou, L., Feng, L.J., Algeo, T.J., Zhang, F.F., Romaniello, S., Jin, C.S., Ling, H.F., Jiang, S.Y., 2017. Transient deep-water oxygenation in the early Cambrian Nanhua Basin, South China. Geochim. Cosmochim. Acta 210, 42–58.
Clarkson, M., Poulton, S., Guilbaud, R., Wood, R., 2014. Assessing the utility of Fe/Al and Fe-speciation to record water column redox conditions in carbonate-rich sediments. Chem. Geol. 382, 111–122.
Compston, W., Zhang, Z., Cooper, J.A., Ma, G., Jenkins, R.J.F., 2008. Further SHRIMP geochronology on the early Cambrian of South China. Am. J. Sci. 308, 399–420.
Cremonese, L., Shields-Zhou, G., Struck, U., Ling, H.-F., Och, L., Chen, X., Li, D., 2013. Marine biogeochemical cycling during the early Cambrian constrained by a nitrogen and organic carbon isotope study of the Xiaotan section, South China. Precambrian Res. 225, 148–165.
Cullers, R.L., Podkovyrov, V.N., 2000. Geochemistry of the Mesoproterozoic Lakhanda shales in southeastern Yakutia, Russia: implications for mineralogical and provenance control, and recycling. Precambrian Res. 104, 77–93.
Dahl, T.W., Connelly, J., Kouchinsky, A., Gill, B., Månsson, S., Bizzarro, M., 2017. Reorganisation of Earth's biogeochemical cycles briefly oxygenated the oceans 520 Myr ago. Geochem. Perspect. 3, 210–220.
Fakhraee, M., Hancisse, O., Canfield, D.E., Crowe, S.A., Katsev, S., 2019. Proterozoic seawater sulfate scarcity and the evolution of ocean–atmosphere chemistry. Nat. Geosci. 12, 375–380.
Fan, R., Deng, S., Zhang, X., 2011. Significant carbon isotope excursions in the Cambrian and their implications for global correlations. Sci. China Earth Sci. 54, 1686–1695.
Fedo, C.M., Wayne Nesbitt, H., Young, G.M., 1995. Unraveling the effects of potassium metasomatism in sedimentary rocks and paleosols, with implications for paleoweathering conditions and provenance. Geology 23, 921–924.
Feng, L., Chao, L., Jing, H., Chang, H., Chu, X., 2014. A sulfate control on marine mid-depth euxinia on the early Cambrian (ca. 529–521 Ma) Yangtze platform, South China. Precambrian Res. 246, 123–133.
Goldberg, T., Strauss, H., Guo, Q., Liu, C., 2007. Reconstructing marine redox conditions for the Early Cambrian Yangtze Platform: evidence from biogenic sulphur and organic carbon isotopes. Palaeogeogr. Palaeoclimatol. Palaeoecol. 254, 175–193.
Guilbaud, R., Slater, B.J., Poulton, S.W., Harvey, T.H., Brocks, J.J., Nettersheim, B.J., Butterfield, N.J., 2018. Oxygen minimum zones in the early Cambrian ocean. Geochem. Perspect. 6, 33–38.
Guo, Q., Strauss, H., Zhu, M., Zhang, J., Yang, X., Lu, M., Zhao, F., 2013. High resolution organic carbon isotope stratigraphy from a slope to basinal setting on the Yangtze Platform, South China: Implications for the Ediacaran–Cambrian transition. Precambrian Res. 225, 209–217.
Habicht, K.S., Gade, M., Thamdrup, B., Berg, P., Canfield, D.E., 2002. Calibration of sulfate levels in the Archean ocean. Science 298, 2372–2374.
Hayashi, K.-I., Fujisawa, H., Holland, H.D., Ohmoto, H., 1997. Geochemistry of ~1.9 Ga sedimentary rocks from northeastern Labrador, Canada. Geochim. Cosmochim. Acta 61, 4115–4137.
He, T., Zhu, M., Mills, B.J., Wynn, P.M., Zhuravlev, A.Y., Tostevin, R., Pogge von Strandmann, P.A.E., Yang, A., Poulton, S.W., Shields, G.A., 2019. Possible links between extreme oxygen perturbations and the Cambrian radiation of animals. Nat. Geosci. 12, 468–474.
Ishikawa, T., Ueno, Y., Komiya, T., Sawaki, Y., Han, J., Shu, D., Li, Y., Maruyama, S., Yoshida, N., 2008. Carbon isotope chemostratigraphy of a Precambrian/Cambrian boundary section in the Three Gorge area, South China: prominent global-scale isotope excursions just before the Cambrian Explosion. Gondwana Res. 14, 193–208.
Jiang, G., Wang, X., Shi, X., Xiao, S., Zhang, S., Dong, J., 2012. The origin of decoupled carbonate and organic carbon isotope signatures in the early Cambrian (ca. 542–520 Ma) Yangtze platform. Earth Planet. Sci. Lett. 317–318, 96–110.
Jiang, S.Y., Yang, J.H., Ling, H.F., Chen, Y.Q., Feng, H.Z., Zhao, K.D., Ni, P., 2007. Extreme enrichment of polymetallic Ni–Mo–PGE–Au in Lower Cambrian black shales of South China: an Os isotope and PGE geochemical investigation. Palaeogeogr. Palaeoclimatol. Palaeoecol. 254, 217–228.
Jin, C., Li, C., Algeo, T.J., Cheng, M., Lei, L., Zhang, Z., Shi, W., 2017. Evidence for marine redox control on spatial colonization of early animals during Cambrian Age 3 (c. 521–514 Ma) in South China. Geol. Mag. 154, 1360–1370.
Jin, C., Li, C., Algeo, T.J., Wu, S., Cheng, M., Zhang, Z., Shi, W., 2020. Controls on organic matter accumulation on the early-Cambrian western Yangtze Platform, South China. Mar. Pet. Geol. 111, 75–87.
Jin, C.S., Li, C., Peng, X.F., Cui, H., Shi, W., Zhang, Z.H., Luo, G.M., Xie, S.C., 2014. Spatiotemporal variability of ocean chemistry in the early Cambrian, South China. Sci. China Earth Sci. 57, 579–591.
Jin, C.S., Li, C., Algeo, T.J., Planavsky, N.J., Cui, H., Yang, X., Zhao, Y., Zhang, X., Xie, S., 2016. A highly redox-heterogeneous ocean in South China during the early Cambrian (~529–514 Ma): Implications for biota-environment co-evolution. Earth Planet. Sci. Lett. 441, 38–51.
Knoll, A.H., Carroll, S.B., 1999. Early animal evolution: emerging views from comparative biology and geology. Science 284, 2129–2137.
Leavitt, W.D., Halevy, I., Bradley, A.S., Johnston, D.T., 2013. Influence of sulfate reduction rates on the Phanerozoic sulfur isotope record. Proc. Natl. Acad. Sci. U. S. A. 110, 11244–11249.
Li, C., Love, G.D., Lyons, T.W., Fike, D.A., Sessions, A.L., Chu, X., 2010. A stratified redox model for the Ediacaran ocean. Science 328, 80–83.
Li, C., Jin, C., Planavsky, N.J., Algeo, T.J., Cheng, M., Yang, X., Zhao, Y., Xie, S., 2017. Coupled oceanic oxygenation and metazoan diversification during the early–middle Cambrian? Geology 45, 743–746.
Li, C., Cheng, M., Algeo, T.J., Xie, S.C., 2015a. A theoretical prediction of chemical zonation in early oceans (> 520 Ma). Sci. China Earth Sci. 58, 1901–1909.
Li, C., Planavsky, N.J., Shi, W., Zhang, Z., Zhou, C., Cheng, M., Tarhan, L.G., Luo, G., Xie, S., 2015b. Ediacaran marine redox heterogeneity and early animal ecosystems. Sci. Rep. 5 art. 17097.
Li, C., Cheng, M., Zhu, M., Lyons, T.W., 2018. Heterogeneous and dynamic marine shelf oxygenation and coupled early animal evolution. Emerg. Top. Life Sci. 2, 279–288.
Liu, Z.H., Zhuang, X.G., Teng, G.E., Xie, X.M., Yin, L.M., Bian, L.Z., Feng, Q.L., Algeo, T.J., 2015. The lower Cambrian Niutitang Formation at Yangtiao (Guizhou, SW China): Organic matter enrichment, source rock potential, and hydrothermal influences. J. Pet. Geol. 38 (4), 411–432.
Loyd, S.J., Marenco, P.J., Hagadorn, J.W., Lyons, T.W., Kaufman, A.J., Sour-Tovar, F., Corsetti, F.A., 2012. Sustained low marine sulfate concentrations from the Neoproterozoic to the Cambrian: Insights from carbonates of northwestern Mexico and eastern California. Earth Planet. Sci. Lett. 339–340, 79–94.
McLennan, S.M., 1993. Weathering and global denudation. J. Geol. 101, 295–303.
McLennan, S.M., 2001. Relationships between the trace element composition of sedimentary rocks and upper continental crust. Geochem. Geophys. Geosyst. 2, 203–236.
McLennan, S.M., Hemming, S., McDaniel, D.K., Hanson, G.N., 1993. Geochemical approaches to sedimentation, provenance, and tectonics. In: Johnsson, M.J., Basu, A. (Eds.), Processes Controlling the Composition of Clastic Sediments. Geological Society of America Special Paper 284. pp. 21–40.
Na, L., Kiessling, W., 2015. Diversity partitioning during the Cambrian radiation. Proc. Natl. Acad. Sci. U. S. A. 112, 4702–4706.
Nursall, J., 1959. Oxygen as a prerequisite to the origin of the Metazoa. Nature 183, 1170–1172.
Och, L.M., Shields-Zhou, G.A., Poulton, S.W., Manning, C., Thirlwall, M.F., Li, D., Chen, X., Ling, H., Osborn, T., Cremonese, L., 2013. Redox changes in Early Cambrian black shales at Xiaotan section, Yunnan Province, South China. Precambrian Res. 225, 166–189.
Okada, Y., Sawaki, Y., Komiya, T., Hirata, T., Takahata, N., Sano, Y., Han, J., Maruyama, S., 2014. New chronological constraints for Cryogenian to Cambrian rocks in the Three Gorges, Weng'an and Chengjiang areas, South China. Gondwana Res. 25, 1027–1044.
Panahi, A., Young, G.M., Rainbird, R.H., 2000. Behavior of major and trace elements (including REE) during Paleoproterozoic pedogenesis and diagenetic alteration of an Archean granite near Ville Marie, Quebec, Canada. Geochim. Cosmochim. Acta 64, 2199–2220.
Peng, S., Babcock, L., Cooper, R., 2012. The Cambrian Period. In: Gradstein, F.M., Ogg, J.G., Schmitz, M., Ogg, G. (Eds.), The Geologic Time Scale 2012. 2. Elsevier, Amsterdam, pp. 437–488.
Poulton, S.W., Canfield, D.E., 2005. Development of a sequential extraction procedure for iron: implications for iron partitioning in continentally derived particulates. Chem. Geol. 214, 209–221.
Poulton, S.W., Canfield, D.E., 2011. Ferruginous conditions: a dominant feature of the ocean through Earth's history. Elements 7, 107–112.
Raiswell, R., Canfield, D.E., 2012. The iron biogeochemical cycle past and present. Geochem. Perspect. 1, 1–220.
Rieu, R., Allen, P.A., Plotze, M., Pettke, T., 2007. Compositional and mineralogical variations in a Neoproterozoic glacially influenced succession, Mirbat area, south Oman: Implications for paleoweathering conditions. Precambrian Res. 154, 248–265.
Sahoo, S.K., Planavsky, N., Jiang, G., Kendall, B., Owens, J., Wang, X., Shi, X., Anbar, A., Lyons, T., 2016. Oceanic oxygenation events in the anoxic Ediacaran ocean. Geobiology 14, 457–468.
Scheffler, K., Buehmann, D., Schwark, L., 2006. Analysis of late Palaeozoic glacial to postglacial sedimentary successions in South Africa by geochemical proxies–Response to climate evolution and sedimentary environment. Palaeogeogr. Palaeoclimatol. Palaeoecol. 240, 184–203.
Schoenborn, W.A., Fedo, C.M., 2011. Provenance and paleoweathering reconstruction of the Neoproterozoic Johnnie Formation, southeastern California. Chem. Geol. 285, 231–255.
Sperling, E.A., Halverson, G.P., Knoll, A.H., Macdonald, F.A., Johnston, D.T., 2013. A basin redox transect at the dawn of animal life. Earth Planet. Sci. Lett. 371–372, 143–155.
Sperling, E.A., Wolock, C.J., Morgan, A.S., Gill, B.C., Kunzmann, M., Halverson, G.P.,

Macdonald, F.A., Knoll, A.H., Johnston, D.T., 2015. Statistical analysis of iron geochemical data suggests limited late Proterozoic oxygenation. Nature 523, 451–454.
Steiner, M., Li, G., Qian, Y., Zhu, M., Erdtmann, B.D., 2007. Neoproterozoic to Early Cambrian small shelly fossil assemblages and a revised biostratigraphic correlation of the Yangtze Platform (China). Palaeogeogr. Palaeoclimatol. Palaeoecol. 254, 67–99.
Stolper, D.A., Keller, C.B., 2018. A record of deep-ocean dissolved O_2 from the oxidation state of iron in submarine basalts. Nature 553, 323–327.
Torres, M.A., Moosdorf, N., Hartmann, J., Adkins, J.F., West, A.J., 2017. Glacial weathering, sulfide oxidation, and global carbon cycle feedbacks. Proc. Natl. Acad. Sci. U. S. A. 114, 8716–8721.
Tribovillard, N., Algeo, T.J., Lyons, T., Riboulleau, A., 2006. Trace metals as paleoredox and paleoproductivity proxies: an update. Chem. Geol. 232, 12–32.
Vannier, J., Liu, J., Lerosey-Aubril, R., Vinther, J., Daley, A.C., 2014. Sophisticated digestive systems in early arthropods. Nat. Commun. 5 art. 3641.
Wang, D., Ling, H.F., Struck, U., Zhu, X.K., Zhu, M., He, T., Yang, B., Gamper, A., Shields, G.A., 2018. Coupling of ocean redox and animal evolution during the Ediacaran-Cambrian transition. Nat. Commun. 9 art. 2575.
Wang, J., Li, Z.X., 2003. History of Neoproterozoic rift basins in South China: implications for Rodinia break-up. Precambrian Res. 122, 141–158.
Wang, J., Chen, D., Yan, D., Wei, H., Xiang, L., 2012. Evolution from an anoxic to oxic deep ocean during the Ediacaran–Cambrian transition and implications for bioradiation. Chem. Geol. 306–307, 129–138.
Wang, W., Guan, C., Hu, Y., Cui, H., Muscente, A.D., Chen, L., Zhou, C., 2020. Spatial and temporal evolution of Ediacaran carbon and sulfur cycles in the Lower Yangtze Block, South China. Palaeogeogr. Palaeoclimatol. Palaeoecol. 537, 109417.
Wang, X., Shi, X., Jiang, G., Zhang, W., 2012. New U–Pb age from the basal Niutitang Formation in South China: Implications for diachronous development and condensation of stratigraphic units across the Yangtze platform at the Ediacaran–Cambrian transition. J. Asian Earth Sci. 48, 1–8.
Wang, Y., Zhang, F., Fan, W., Zhang, G., Chen, S., Cawood, P.A., Zhang, A., 2010. Tectonic setting of the South China Block in the early Paleozoic: Resolving intracontinental and ocean closure models from detrital zircon U-Pb geochronology. Tectonics 29, art. TC6020.
Wei, G.-Y., Planavsky, N.J., Tarhan, L.G., Chen, X., Wei, W., Li, D., Ling, H.-F., 2018. Marine redox fluctuation as a potential trigger for the Cambrian explosion. Geology 46, 587–590.
Wen, H., Carignan, J., Chu, X., Fan, H., Cloquet, C., Jing, H., Zhang, Y., Chang, H., 2014. Selenium isotopes trace anoxic and ferruginous seawater conditions in the Early Cambrian. Chem. Geol. 390, 164–172.
Xiang, L., Schoepfer, S.D., Shen, S.Z., Cao, C.Q., Zhang, H., 2017. Evolution of oceanic molybdenum and uranium reservoir size around the Ediacaran–Cambrian transition: evidence from western Zhejiang, South China. Earth Planet. Sci. Lett. 464, 84–94.
Yan, D., Chen, D., Wang, Z., Li, J., Yang, X., Zhang, B., 2019. Climatic and oceanic controlled deposition of Late Ordovician-Early Silurian black shales on the North Yangtze platform, South China. Mar. Pet. Geol. 110, 112–121.
Yang, A., Zhu, M., Zhang, J., Li, G., 2003. Early Cambrian eodiscoid trilobites of the Yangtze Platform and their stratigraphic implications. Prog. Nat. Sci. 13, 861–866.
Yang, B., Steiner, M., Zhu, M., Li, G., Liu, J., Liu, P., 2016. Transitional Ediacaran–Cambrian small skeletal fossil assemblages from South China and Kazakhstan: Implications for chronostratigraphy and metazoan evolution. Precambrian Res. 285, 202–215.
Yao, W.-H., Li, Z.-X., Li, W.-X., Li, X.-H., Yang, J.-H., 2014. From Rodinia to Gondwanaland: a tale of detrital zircon provenance analyses from the southern Nanhua Basin, South China. Am. J. Sci. 314, 278–313.
Yao, W.-H., Li, Z.-X., Li, W.-X., 2015. Was there a Cambrian ocean in South China? –Insight from detrital provenance analyses. Geol. Mag. 152, 184–191.
Yuan, J.L., Zhao, Y.L., 1999. Subdivision and correlation of Lower Cambrian in southwest China, with a discussion of the age of Early Cambrian series biota. Acta Micropalaeontol. Sin. 38 (Sup.), 116–131 (in Chinese with English abstract).
Zhai, L., Wu, C., Ye, Y., Zhang, S., Wang, Y., 2018. Fluctuations in chemical weathering on the Yangtze Block during the Ediacaran–Cambrian transition: Implications for paleoclimatic conditions and the marine carbon cycle. Palaeogeogr. Palaeoclimatol. Palaeoecol. 490, 280–292.
Zhang, S., Li, H., Jiang, G., Evans, D.A.D., Dong, J., Wu, H., Yang, T., Liu, P., Xiao, Q., 2015. New paleomagnetic results from the Ediacaran Doushantuo Formation in South China and their paleogeographic implications. Precambrian Res. 259, 130–142.
Zhang, Z., Li, C., Cheng, M., Algeo, T.J., Jin, C., Tang, F., Huang, J., 2018. Evidence for highly complex redox conditions and strong water-column stratification in an early Cambrian continental-margin sea. Geochem. Geophys. Geosyst. 19, 2397–2410.
Zhu, M.Y., 2010. The origin and Cambrian explosion of animals: fossil evidence from China. Acta Palaeontol. Sin. 49, 269–287 (in Chinese with English abstract).
Zhu, M.Y., Li, G.X., ZHANG, J.M., Steiner, M., Qian, Y., Jiang, Z.W., 2001. Early Cambrian stratigraphy of East Yunnan, southwestern China: a synthesis. Acta Palaeontol. Sin. 40, 4–39.
Zhu, M.Y., Zhang, J., Steiner, M., Yang, A., Li, G., Erdtmann, B., 2003. Sinian-Cambrian stratigraphic framework for shallow-to deep-water environments of the Yangtze Platform: an integrated approach. Prog. Nat. Sci. 13, 951–960.
Zhu, M.Y., Zhang, J., Yang, A., 2007. Integrated Ediacaran (Sinian) chronostratigraphy of South China. Palaeogeogr. Palaeoclimatol. Palaeoecol. 254, 7–61.
Zhu, M.Y., Zhang, J., Yang, A., Li, G., Zhao, F., Lu, M., Yin, Z., 2016. Stratigraphic and depositional frameworks of the Neoproterozoic source-reservoir-cap rock associations in South China. In: Sun, S., Wang, T. (Eds.), Geology and Hydrocarbon Resources of the Middle-Upper Proterozoic in East China. Science Press, Beijing, pp. 107–135.